Chapter 3
InAs/GaAs Quantum Dots with Multimodal Size Distribution

Udo W. Pohl

3.1 Introduction

Semiconductor research and applications have experienced a progressive reduction in dimensionality of structures from bulk, through quantum wells and wires to quantum dots (QDs). QDs provide an ultimate limit of charge carrier confinement. Their size is in the nanometer range, i.e. of the order of the exciton Bohr radius, giving rise to fully quantized confined electron and hole states. Their electronic properties differ significantly from those of systems with higher dimensionality and offer potential applications in novel optoelectronic devices.

The most effective method for the fabrication of coherent, dislocation-free semiconductor QDs is the strained-layer epitaxy in the Stranski–Krastanow mode [1, 2]. Such self-organized transformation from two-dimensional layer-by-layer growth to a three-dimensional mode was found for many heterostructure systems. InAs quantum dots in GaAs matrix represent the best studied model system. The discrete energy states and the ease of integration into an optoelectronic device recently lead, e.g., to the presentation of electrically driven single photon sources [3]. Prerequisite for practical applications is the ability to control the electronic properties of the dot. Fabrication of quantum dots by applying Stranski-Krastanow growth is hampered by the action of entropy at growth temperature, usually leading to ensembles of dots which vary in size, shape, and composition. Consequently the energies of bound states vary within the ensemble. Since this growth mode still yields defect-free dots with superior electronic properties, the technique was recently advanced to improve the shape homogeneity within the ensemble and the integrity of the dot-matrix interfaces [4]. The development aimed to find a growth regime which simultaneously favors the formation of equilibrium-near dots with homogeneous composition and sharp interfaces. This chapter addresses the growth control of such particular kind of InAs dots in GaAs matrix and their electronic properties.

Z. M. Wang, *Self-Assembled Quantum Dots.*

© Springer 2008

3.2 Decomposition of the Size Distribution into Subensembles

An ensemble of self-organized QDs usually contains a broad distribution of QD sizes, often accompanied by a spread of QD's compositions due to intermixture with matrix material. These fluctuations of single QD properties lead to a statistical distribution of the eigenenergies within the ensemble. Consequently, the luminescence of the QD ensemble is a convolution of sharp single QD spectra with the distribution function [5], typically yielding an inhomogeneously broadened band with a gaussian shape of up to 100 meV half width. An early study on chemical beam epitaxy of strained InAs quantum wells in InP matrix indicated the existence of a growth regime which simultaneously produces equilibrium-near non-intermixed dots and sharp interfaces [6]. The introduction of a growth interruption (GRI) after InAs deposition and prior to InP cap layer growth lead to layers which show up to eight well separated emission lines. The lines were attributed to one-monolayer (ML) thickness fluctuations of the InAs/InP well, as previously also reported for lattice-matched materials GaAs/AlGaAs and InP/GaInAs. The interpretation was improved later, stating that three-dimensional islands with heights corresponding to integral numbers of InAs MLs form under the given growth conditions [7, 8].

More recent studies on the Stranski-Krastanow growth of InAs demonstrated that such growth regime also exists for QD formation in GaAs matrix and proved the dot height quantization. Figure 3.1 shows PL spectra of two samples with thin InAs layers in GaAs, grown using metalorganic vapor phase epitaxy. In one sample the GaAs cap layer was immediately grown after the deposition of the InAs layer, in the other sample a short growth interruption was introduced prior to GaAs cap deposition, keeping other growth parameters unchanged. The first sample shows a narrow PL which corresponds to an e_0-hh_0 exciton recombination in a pseudomorhic InAs/GaAs quantum well of ∼1.8 ML thickness, in good agreement with the amount of deposited material. The asymmetry at the low-energy side is well

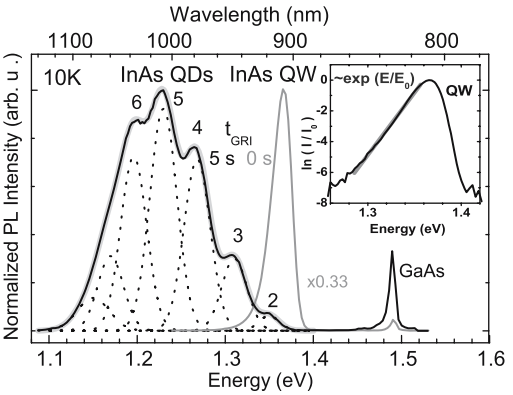

Fig. 3.1 PL spectra of InAs/GaAs samples grown without (grey curve) and with $t_{GRI} = 5$ s growth interruption. The thick grey curve is the sum of the dotted Gaussian fits, GaAs denotes matrix near band-edge emission. The inset shows the QW spectrum in a semilogarithmic scale. After [4], inset from [9]

described by an exponential function $I \propto \exp(E/E_0)$, cf. inset in Fig. 3.1. The dependence indicates quantum well (QW) states with a density-of-states tail originating from potential fluctuations due to thickness variations [9]. This proves the formation of a rough InAs/GaAs quantum well if no GRI is applied.

The sample grown with an additional growth interruption of 5s clearly shows PL of a QD ensemble peaking near 1.2 eV. The apparent modulation of the QD-ensemble emission originates from the decomposition into narrow emission lines of subensemles. The subensembles are related to InAs QDs which differ in height by one InAs ML [4, 10]. The numbers on the peaks in Fig. 3.1 mark the heights of the respective subensemble QDs in ML units. The multimodal nature of the ensemble size-distribution was concluded from a combined structural, optical, and theoretical study described in more detail in the following sections.

3.2.1 Initial Stages of Dot Formation

If InAs is deposited on GaAs instead of InP the strain is nearly doubled. The critical layer thickness for elastic strain relaxation in Stranski-Krastanow growth is hence reduced. A critical value near only 1.5 ML [2] leads to the requirement of an atomically flat GaAs surface prior to InAs deposition to obtain well-defined bottom interfaces of the dots. This is easily achieved by an appropriate process [11]. The InAs/InP islands were reported to form from a two-dimensional InAs layer during the growth interruption [6]. This means that the deposited amount of InAs was close to the critical value for the Stranski-Krastanow transition on InP. To study the respective conditions for deposition on GaAs, transients of the anisotropic reflectance were recorded in-situ during the growth of In(Ga)As layers with strain below and just above the critical value for elastic relaxation. A fixed photon enery of 2.6 eV was selected due to its high surface sensivity [12]. The Stranski-Krastanow transition was retarded by composition with Ga to reduce the strain in the layers. This allowed for optically tracing the response during deposition. Transients of reflection anisotropy-spectra (RAS) of such InGaAs/GaAs layers show oscillations, which are particularly pronounced at high Ga composition, cf. Fig. 3.2. The oscillations originate from reconstruction domains of reduced As coverage close to monolayer steps which occur in the island growth mode at the low deposition temperature used for dot growth [13]. The damping of the modulation for increasing In content is attributed to a combined effect of a more group-III-rich surface due to the reduced As-In bond strength as compared to Ga-As and that of a transition to step-flow growth due to the higher surface mobility of In species as compared to Ga.

The InGaAs layer with 65% Ga exceeds the critical strain for dot formation. The respective RAS signal shows just two monolayer oscillations. Dot formation does not lead to a clear feature in the response. The apparent drop is related to a slight depletion of As at the surface due to an interruption of As precursor supply during GRI. The RAS response during GRI basically originates from the In(Ga)As wetting

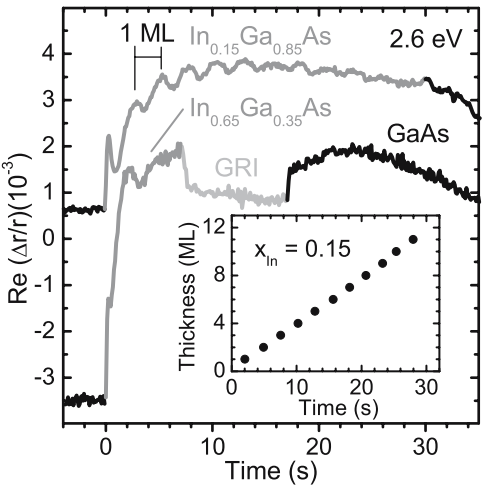

Fig. 3.2 Transients of the anisotropic reflectance recorded during metalorganic vapor phase epitaxy of InGaAs layers with different In compositions on GaAs at 485°C. GRI denotes a growth interruption without precursor supply. The inset shows the temporal thickness increase in units of monolayers. From [27]

layer, the slow changes are assigned to an optically detected coarsening due to dot ripening. The in-situ RAS study clearly demonstrates that a smooth growth front is maintained during strained layer deposition on GaAs prior to dot formation.

The in situ study indicates that comparable conditions as reported for InAs on InP are hence also given for the deposition of InAs on GaAs, encouraging growth of a multimodal QD ensemble. To induce such QD formation, ∼1.9 ML thick InAs layers were deposited at typ. 490°C with a comparatively high deposition rate of 0.4 ML/s. Growth interruptions of variable duration were applied after InAs deposition and prior to GaAs cap layer deposition, showing a strong effect on the structural and optical properties of the layers [4, 9]. The PL of a sample series grown with gradually prolonged duration of short growth interruptions shows how the multimodal dot ensemble forms from the initial rough QW, cf. Fig. 3.3. Without interruption a PL maximum at 1.38 eV is found, corresponding to the exciton recombination in a QW. Comparison of the low-energy emission tail with the peak-energy separations of QD subensembles indicates significant localization in the DOS of the QW and a related strong roughness. Application of a 0.5s growth interruption leads to a small blue shift of the PL maximum and some broad emission band around 1.3 eV. These features originate from thinning of the QW and an enhanced appearance of locally thicker parts of the QW. The blue shift of the QW-related PL saturates for longer interruptions, and the emission of a multimodal QD ensemble with individual subensemble peaks evolves from the shallow localizations in the DOS tail of the rough QW. The material of the initial InAs deposition hence partially concentrates at some QD precursors of dots located on a wetting layer of contant thickness. The existence of such a constant, 1 monolayer thick wetting layer consisting of pure InAs was proved by PL excitation studies discussed below and confirmed by TEM investigations [4].

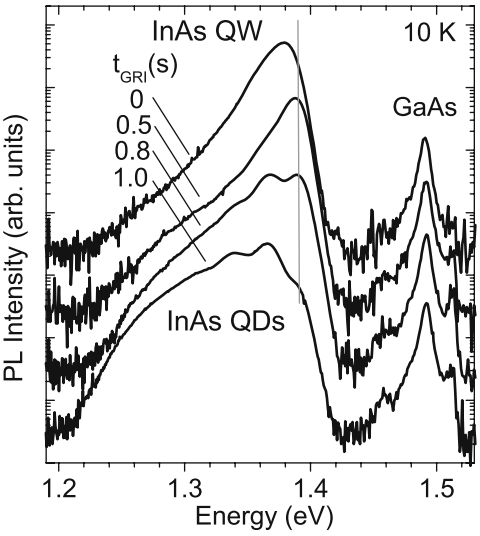

Fig. 3.3 PL spectra of InAs/GaAs layers grown with different durations t_{GRI} of short growth interruptions prior to GaAs cap layer deposition. Curves are vertically shifted by one decade for clarity, the grey vertical line is a guide to the eye. From [27]

3.2.2 Evolution of the Dot-Size Distribution

The detection of the quantization of dot heights within a multimodal ensemble provides a sensitive tool to trace the ripening of dots during the growth interruption. For longer GRI durations the PL energy of the QD ensemble shifts to lower energy due to an average dot-size increase. The emission lines of individual subensembles do *not* shift to the red. The lines rather shift to the blue as shown in Fig. 3.4 by comparing, e.g., corresponding emissions of samples grown with 2 s and 10 s GRI. Since the height of QDs in a given ensemble remains constant for varied GRIs the shift indicates a lateral dissolution of subensembles of smaller dots and a materials redistribution to form subensembles of larger dots. PL excitation spectra recorded in the respective maxima of samples grown with different GRIs show heavy hole and light hole exciton-resonances of the wetting layer QW remaining at fixed energies for all samples, cf. Fig. 3.4c. Thickness and composition of the wetting layer consequently remain unchanged during the ripening of the dots. The *hh* and *lh* exciton transition energies correspond to a QW of 1 ML thickness and pure InAs composition. This means that the evolution of the QD ensemble proceeds solely by mass transport among the dots.

The dynamics of evolution is revealed by analyzing the integral PL intensity of individual subensembles at various stages of the evolution shown in Fig. 3.4. Model calculations of excitons confined in dots of varied sizes show that the relative oscillator strength of the emission is largely insensitive to the size of the QDs [14]. The integral intensity of the subensemble peaks is hence considered a reasonable direct measure for the number of QDs with a specific corresponding height.

The temporal evolution of these intensities given in Fig. 3.5 directly shows the formation of subensembles with larger dots by dissolution of the subensembles built

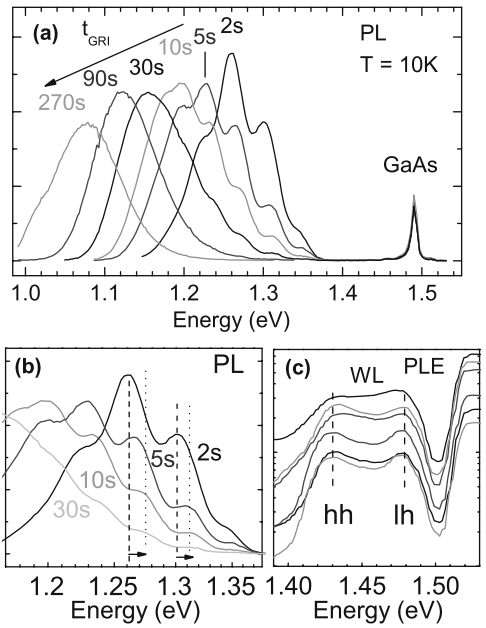

Fig. 3.4 PL (a, b) and PL excitation spectra (c) of InAs/GaAs samples with multimodal QDs grown with varied growth interruptions t_{GRI}. WL denotes the wetting layer with resonances of the heavy hole and light hole. (a) and (c) from [4]

by smaller dots. The number of, e.g., dots with 5 ML height increases during the initial 5s growth interruption on expense of those with 2 to 4 ML height. Then the number of these dots decreases – either by dissolution to provide material to increase the number of 6 ML high dots, or by growth. After 10s GRI also the 6 ML high dots start to dissolve.

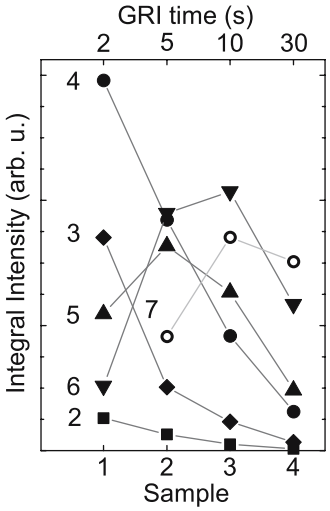

Fig. 3.5 Integral PL intensities of subensemble peaks measured from samples grown with various growth interruptions. The numbers refer to QD heights in monolayer units as indicated in Fig. 3.1. From [14]

3.2.3 Structural Properties of Multimodal InAs/GaAs Dots

The assignment of the modulation observed in the PL of the dot ensemble (Fig. 3.1) to a discretization of dot heights and a consequential decomposition of the ensemble into subensembles is substantiated by cross-sectional transmission-electron micrographs. The images shown in Figs. 3.6 and 3.7 were recorded along (100) using the strain sensitive (220) reflections, the chemically sensitive (200) reflections, and the direct beam. InAs dots then appear as bright central areas, as shown in the overview Fig. 3.6. The dark areas above the dots – for larger dots also below – correlate to strain fields in the surrounding GaAs matrix. The dots have a low aspect ratio with flat top and bottom facets. Their lateral extension is about 10 nm.

Details of the dot shape are obtained from high resolution images. The local chemical composition is obtained from Fourier-filtered images using the {200} components and the transmitted beam in the reconstruction. Figure 3.7 shows a HRTEM image of a dot and the result of such image processing. The crystal lattices of the InAs dot and the GaAs lattice are apparently different and allow for a quantitative analysis. The base and the top layer of the flat dots consist of plain, continuous InAs, forming atomically sharp interfaces to the cladding GaAs matrix. No significant InAs-GaAs intermixing is found. The dots consequently differ in height by integer numbers of InAs monolayers. The side facets are less well resolved in the images, due to high strain perturbations at the base perimeter of the QDs. They appear as steeply inclined facets, giving the QDs a shape of a truncated pyramid. Such a result was also observed in cross-section scanning tunneling images of multimodal InAs/GaAs QDs [15], see top image in Fig. 3.7. The filled-state STM image shows horizontal lines due to the III-V zigzag chains at the scanned zincblende (110) surface, one such line corresponds to two atomic monolayers. Dots appear as bright contrast with sharp interfaces to the matrix, confirming flat top and bottom facets built of pure InAs.

Theoretical studies on the shape of InAs/GaAs dots were reported particularly for uncovered or partially covered structures. Truncated pyramids with flat top and bottom facets, as found for the covered InAs/GaAs QDs studied here, agree with predictions [16, 17] and findings [18] of equilibrium shapes of uncovered dots. The observation of truncated pyramidal shape for *covered* dots is in agreement with a recent STM study on the capping of free standing InAs dots [19]. During the initial stages of cap-layer deposition the dots rapidly shrink vertically, building flat structures which are close to equilibrium shapes.

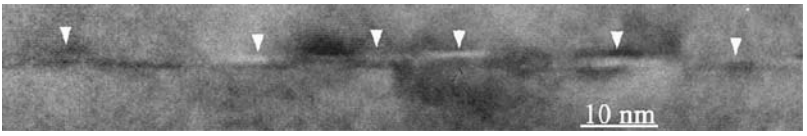

Fig. 3.6 Cross section transmission electron micrograph of InAs/GaAs dots growth with 5 s GRI, imaged along [100] using strain and chemically sensitive reflections. White arrows mark areas with contrast changes due to flat dots

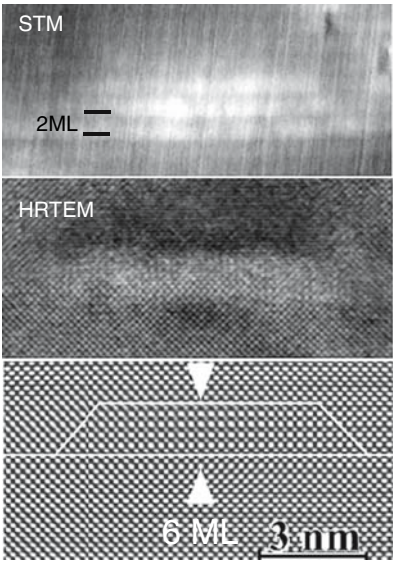

Fig. 3.7 Cross-section scanning tunneling (top) and high resolution transmission-electron micrograph (middle) of InAs/GaAs QDs with 6 ML height. Bottom: Fourier-filtered image of the HRTEM micrograph. Top image from [15], middle and bottom from [4]

The evolution of the dot ensemble by dissolution of small dots described in Section 3.2.2 is also reflected in the QD areal density. Plain view bright-field TEM images given in Fig. 3.8 show that the QD density decreases from $4.0 \times 10^{10}\,\mathrm{cm}^{-2}$ for 5s growth interruption to $1.7 \times 10^{10}\,\mathrm{cm}^{-2}$ for 90s [4]. The simultaneously increased sizes of the dots induce larger strain fields. This leads to higher contrast in the images recorded using the strain-sensitive (220) reflection and slightly off-axis two-beam conditions (images for 5s and 90s GRI). The black-white contrast in these images is oriented along the (220) diffraction vector. No dislocated islands were observed in the samples, except for the longest GRI of 270s where a high density of misfit dislocations ($1.9 \times 10^{8}\,\mathrm{cm}^{-2}$) which originate at InAs islands was found. For such samples containing dislocated islands, the investigation of strained-QD evolution is complicated due to a faster growth of relaxed islands, i.e. an increased material transfer to these regions [20]. The density of not dislocated dots has then consequently dropped, in this sample to $0.9 \times 10^{10}\,\mathrm{cm}^{-2}$. The study of coherently strained dots did hence not include such long growth interruptions.

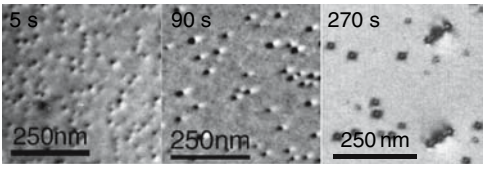

Fig. 3.8 Plan view transmission-electron micrographs of InAs/GaAs QD samples grown with different growth interruptions as indicated. From [4]

3.2.4 Kinetic Model of Multimodal Dot Ensembles

The formation of a dot ensemble with a multimodal size distribution may theoretically be described using a kinetic approach [4, 14]. The model outlined in Fig. 3.9 assumes strained dots of truncated pyramidal shape being surrounded by an adatom sea which represents the InAs wetting layer. Growth and dissolution of a dot occurs by attachment and detachment of adatoms. The kinetics is basically controlled by the stress which is concentrated at the base perimeter of a dot. There the dot's elastic energy creates a barrier for the nucleation at the side facets. The barrier increases with the height of a dot. Therefore growth by adding new layers on the top facet is favored, keeping the dot base constant. Material for growth is provided from dissolution of smaller dots.

A partially grown layer on the top facet of a dot leads to a change of the Gibbs free energy of the system, given by

$$\delta\Phi_{dot} = \delta E_{elast} + \delta E_{edge} - \mu\delta N \tag{3.1}$$

δE_{elast} is the elastic relaxation-energy change and leads to a decrease of Gibbs free energy as the number of atoms in the dot increases. δE_{edge} is the step energy of the additional partial layer on the top facet and increases with the length of its perimeter. δN is the number of atoms in the partial layer, that are transferred from the adatom sea. μ is the chemical potential of the adatom sea. $\delta\Phi_{\mathrm{dot}} > 0$ at the initial growth stage of an additional layer, but eventually becomes negative when this layer exceeds a critical size. Gibbs free energy then decreases if the dot grows. Each time a top layer of a dot is completed the Gibbs free energy has local minimum, cf. Fig. 3.10. Since the size of the top facet of the truncated pyramid decreases with height, it will at a certain height become too small to further favor formation of a subsequent layer. Growth of this dot will then stop. QDs with larger initial bases will therefore stop growing at a larger height.

For numerical modeling, the exchange of adatoms between sea and dot is described by rate equations [14]. An Arrhenius dependence in the probability of

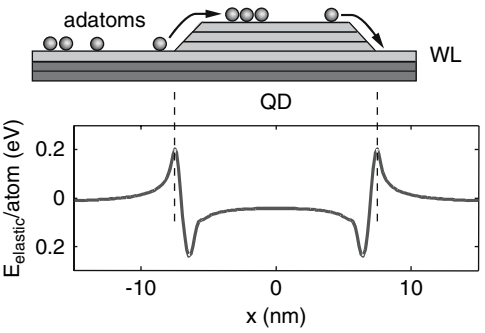

Fig. 3.9 Model of an InAs dot on a 1 ML thick wetting layer. Bottom: Elastic energy density of the dot

dot-height increase or decrease $W\,(b, h \rightarrow h \pm 1)$ accounts for the strain-dependent barrier,

$$W\,(b, h \rightarrow h \pm 1) = \omega\, \exp(-\delta\Phi_{barrier}/k_B T). \tag{3.2}$$

An equal prefactor ω is assumed for all dots. The temporal evolution of the dot heights h and base lenths b in the ensemble is described by the distribution function $F(b, h, t)$ which obeys a master equation

$$\frac{\partial F}{\partial t} = \sum W \times F, \tag{3.3}$$

with a sum over all height increases ($h-1 \rightarrow h$ and $h \rightarrow h+1$) and decreases ($h+1 \rightarrow h$ and $h \rightarrow h-1$). Growth or dissolution of the dots proceeds by mass exchange between the dots and the adatom sea. For the growth interruption, the mass conservation criterion reads

$$q_{\text{adatom}}(t) + \sum_b \sum_h F(b, h, t)\, V(b, h) = Q = const. \tag{3.4}$$

The number of adatoms q_{adatom} in the adatom sea decreases as a dots grows, thereby lowering the chemical potential μ due to the relation

$$q_{\text{adatom}} \propto \exp(\mu/(k_B T)), \tag{3.5}$$

and consequently raising $\delta\Phi_{\text{dot}}$. An increase of Gibbs free energy leads at an early stage of evolution (μ_1) to a larger critical size of the additional layer on top of a dot, see Fig. 3.10. At a later stage (μ_2) both growth of high dots and dissolution of small dots lead to a decrease of the free energy. The driving force for dissolution acts inverse to that of growth, i.e. predominantly at the respective topmost layer of

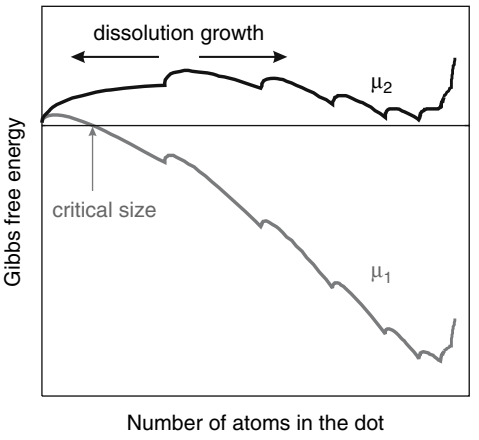

Fig. 3.10 Gibbs free energy of a dot with truncated pyramid shape due to consecutive growth of layers on the top facet. Grey and black curves refer to adatom sea chemical potentials at an early (μ_1) and a later stage ($\mu_2 < \mu_1$) of the evolution, respectively. From [4]

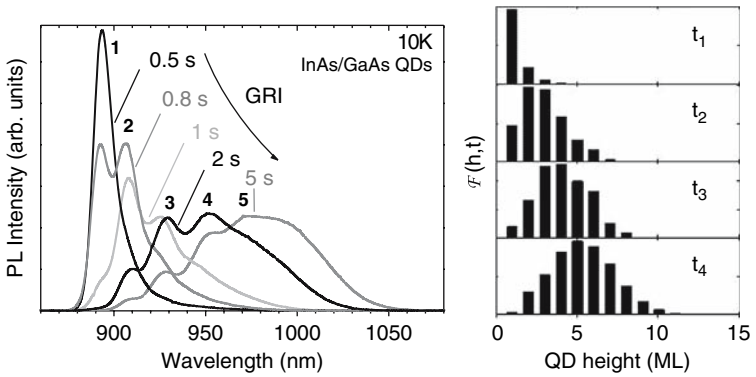

Fig. 3.11 Measured (left panel) and simulated initial stages (right panel) of the evolution of a dot ensemble with a multimodal size distribution

the top facet. Therefore small dots are expected to dissolve by a reduction of height, feeding their material to the adatom sea. Parameters to account for δE_{elast} and δE_{edge} of InAs/GaAs dots were adopted from continuum elasticity and density-functional theory, respectively.

Results of a numerical solution of the coupled set of Eqs. (3.3) to (3.5) are given in Fig. 3.11 for different stages of the evolution [14]. The simulated ensemble initially consists of 1 ML high dots and some minor contributions of higher dots. These dots have a broad distribution of base lengths b. At later stages the number of 1 ML high dots gradually decreases and the maximum of the distribution function F shifts towards higher dots by either dissolution or enlargement of more shallow dots. The model accounts for major features of the experimental data: Formation of a dot ensemble with a multimodal size distribution, an evolution by dissolution of smaller and growth of larger dots, dissolution of the dots by reduction of height, and the persistence of a flat top facet.

3.3 Electronic Properties of Multimodal InAs/GaAs Dots

The detailed knowledge about the structural properties of InAs/GaAs quantum dots in an ensemble with a multimodal size distribution provides an excellent opportunity to study the complex interplay of Coulomb interaction and external confinement for confined charge carriers. The equally shaped dots with well-defined sizes allow for a direct correlation of structural and optical properties, and an analysis of the origin of excitonic properties by realistic model calculations.

3.3.1 Size-dependent Energy Levels

Generally differences in the size of QDs lead to a spread of optical transition energies within a QD ensemble. The apparent decomposition of the ensemble PL into

subensemble emissions shows that the statistical deviations around the mean values within a subensemble are smaller than the differences of the mean values of adjacent subensembles. Spectral broadening of a given subensemble due to variations of QD base length, remaining interface roughness and composition fluctuations is hence smaller than the energy shift caused by the addition of one InAs monolayer to the height. The energy shift between subsequent subensemble maxima is expected to decrease with increasing height, in qualitative agreement with the experiment. The shifts of the emissions depicted in Fig. 3.1 descease from ∼40 meV for shallow dots to 30 meV with increasing height. The effect of monolayer splitting is even more pronounced if antimony is added during formation of the dots, acting as a surfactant and leading to smoother interfaces [4, 10]. In the following such a sample is used to prove that the spectral separation of subensemble emission maxima is due to a discrete variation of QD height in steps of InAs monolayers, accompanied by a simultaneous increase in base length.

The photoluminescence of an InAs/GaAs QD ensemble with a pronounced multimodal size distribution is given in Fig. 3.12 [21]. An excitation density below 4 mW/cm^{-2} ensured an average occupation below one exciton per dot, excluding the occupation of exited states. This is confirmed by PLE spectra Fig. 3.13 which do not show excitation transitions corresponding to emissions in the PL spectrum.

The PL spectrum shows excitonic ground-state emissions of eight subensembles with mutual energy spacings from 51 to 29 meV with increasing QD height. The

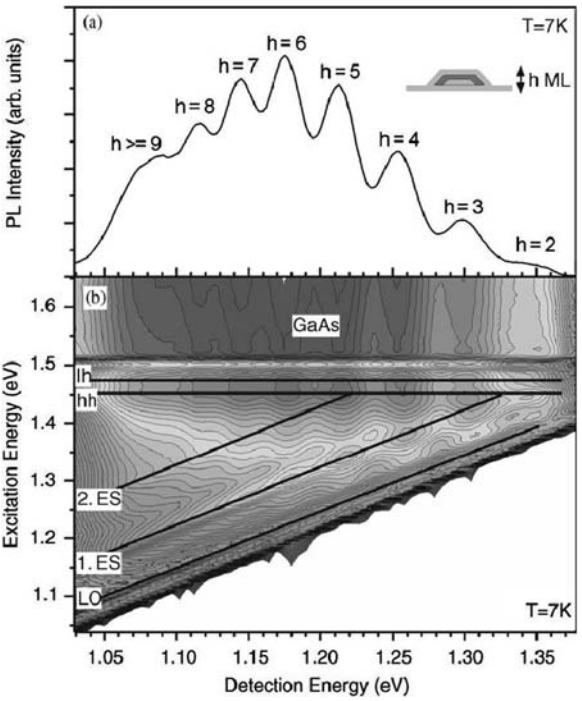

Fig. 3.12 PL spectrum (a) and PLE contour plot (b) of an InAs/GaAs QD ensemble with multimodal size distribution. Horizontal black lines indicate light-hole (*lh*) and heavy-hole (*hh*) resonances of the wetting layer, inclined lines mark the first and second excited QD level and the 1-LO phonon transition. From [21]

emission energy of a subensemble with a given height is smaller than that found in samples grown without antimony, cf. Fig. 3.1. This indicates a larger lateral extension of the QDs formed under mediation of Sb.

The excited exciton states of the QDs are assessed by PLE spectra. Figure 3.12b displays the PL intensity on a logarithmic scale as a function of both detection and excitation energies. The resonance of the heavy-hole exciton in the wetting layer at 1.45 eV marks the onset of the excitation continuum that limits the localization in the QDs. Due to this common resonance for all QDs in the ensemble exciton localization decreases from ∼360 meV for high QDs to ∼100 meV for shallow QDs with 2 ML height. QDs with a ground-state transition energy below 1.22 eV have at least two excited states (1.ES and 2.ES), whereas smaller QDs with transition energies between 1.22 eV and 1.32 eV have only one. Quantum dots with transition energies above 1.32 eV have no bound excited state.

Transitions into excited states are also clearly resolved in the PLE spectra given in Fig. 3.13. They reveal the first excited state about 120 meV above the ground state. Such large substate splitting supports a high InAs content in small QDs. The quantization of the very shallow QDs with 3 and 2 ML height apparently decreases. This effect is attributed to delocalization of the first excited state into the wetting layer.

Based on the structural data of the QDs presented in Section 2.3 the energy of excitons confined in such truncated pyramidal InAs dots was calculated [10, 22, 23]. The three-dimensional model used 8-band **k.p** theory and included a configuration interaction scheme. The **k.p** method is based on the envelope-function ansatz of Bloch's theorem, stating that the electron (or hole) wave function in a crystal with translational symmetry can be separated into a Bloch part and an envelope part. The Bloch part oscillates with the atomic distance as period, while the smooth envelope function only varies on mesoscopic distances. The oscillating Bloch functions can be eliminated from the electron Hamiltonian, leaving eigen-equations of the

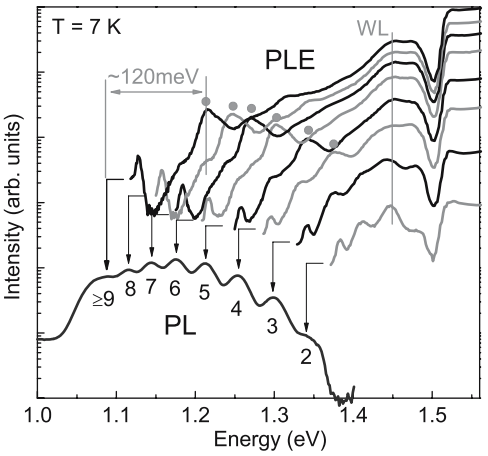

Fig. 3.13 PL and PLE spectra of the InAs/GaAs QD sample which is also measured in Fig. 3.12. Arrows mark maxima of the detection energies of the PLE spectra. From [10]

envelope functions only. In a zincblende semiconductor the single-particle wave function Ψ (**r**) is given by

$$\Psi(\mathbf{r}) = \sum_{\mathrm{R}} \sum_{i=1}^{8} \psi_i(\mathbf{R}) w_i(\mathbf{r} - \mathbf{R}), \tag{3.6}$$

ψ being the 8-dimensional envelope part determining the amplitude of Ψ at the locations **R** of the atoms, and w_i is the Wannier (Bloch) part featuring the *S* or *P* character. The eight enveloppe functions of ψ belong to the electron of the lowest conduction band, the heavy hole, the light hole, and the split-off hole of the uppermost valence band for the two orientations of the spin, respectively. Two-particle exciton energies are calculated using the configuration-interaction (CI) method, including excited-state configurations in the basis set [23]. Modeling thus accounts for direct Coulomb interaction, correlation and exchange. Since both the structure and the size of the studied InAs/GaAs QDs are well known due to their multimodal nature and all prominent interactions are included, the modeling provides a realistic picture of the confined particle's properties. Modeling starts assuming shape, size and composition of a QD. Then the strain distribution and the consequential piezoelectric potential are calculated [24]. Solution of the Schrödinger equation with these potentials yields the single-particle wave-functions. Parameters for the calculation are taken from experimental values for the bulk material Γ-point band structure. It should be noted that the model does not contain adjustable parameters. Excitonic properties are finally calculated in the basis of the single-particle states and the mentioned interaction schemes.

The outlined calculation was applied to pure InAs/GaAs QDs with truncated pyramid shape, (001) bottom and top facets, and {110} side facets. In the model an additional 1 ML thick InAs wetting layer is assumed, in agreement with the heavy- and light-hole energies observed in the PLE spectra. The calculation leads to a good agreement to the experimental results if an appropriate base length is assumed. The energies of the ground and excited states in a small QD of 3 ML height are well explained, if a base length of 10.2 nm is used, see Fig. 3.14. However, keeping this base length for higher dots results in too high predicted transition energies. Similarly energies of a 9 ML high dot are well explained using 13.6 nm base length, but such base length yields too low predicted energies for smaller dots. Consequently both, height and base length actually increase for larger dots, as proved by the excellent agreement of the calculated energies connected by the black lines in Fig. 3.14. Quantum dots in the ensemble with a multimodal size distribution hence show a gradual shell-like increase in volume.

In section 3.2 the dynamics of QD evolution was assessed using the integral intensities of the subensemble emissions. This approach is justified by a calculation of the relative oscillator strength, proving that this quantity is insensitive to the size of the QDs. As shown in Fig. 3.15 the calculated ground-state wave-functions of electron and hole do not vary strongly if height and base length of a QD are changed from 3 ML / 10.2 nm to 13 ML / 15.8 nm, respectively. Consequently the overlap

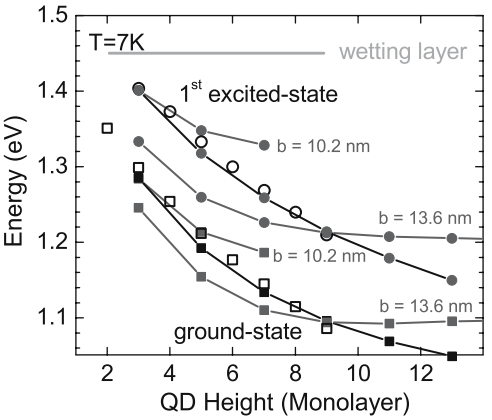

Fig. 3.14 Calculated (solid symbols) and experimental (open symbols) energies of the exciton ground state (squares) and first excited state (circles) for truncated pyramidal InAs QDs. Black lines connect calculated data for varied base length b. From [10]

hardly changes for QDs considered here. In the strong-confinement regime the oscillator strength of the ground-state transition is ruled solely by the ground-state electron-hole overlap [25]. Even the largest QDs still provide a strong confinement, electron and hole wave-functions are hence spatially squeezed.

3.3.2 Binding Energy of Confined Exciton Complexes

For an engineering of quantum dots as building blocks in novel applications knowledge about the electronic structure of few-particle states and the relation of struc-

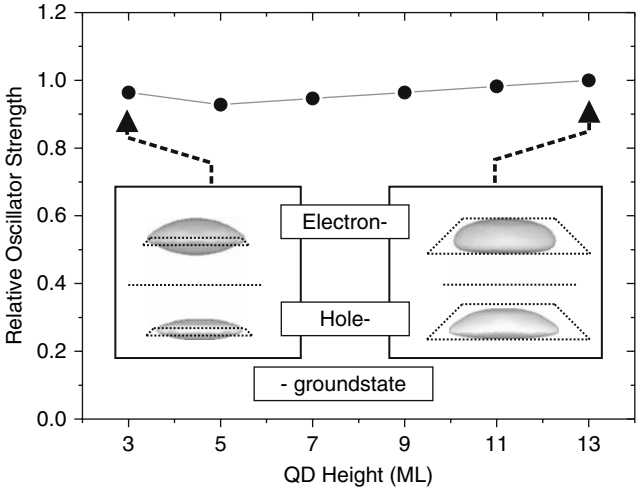

Fig. 3.15 Relative oscillator strength of the exciton emission in an InAs/GaAs QD of truncated pyramid shape. The inset shows calculated e_0 and hh_0 wave functions for 3 ML high QDs (left) and 13 ML high QDs. From [14]

tural and electronic properties is essential. Inhomogeneous broadening of the QD ensemble or subensemble is generally much larger than energy differences between states of various excitonic complexes or exchange energies. Therefore single-QD spectroscopy has been established as a powerful tool to study few-particle effects by excluding influences of inhomogeneous broadening. Results presented below were obtained using spatially resolved cathodoluminescence (CL) with an optically opaque near-field shadow-mask made of Au, which is evaporated onto the sample surface to reduce the number of simultaneously probed dots. For $\sim$100 nm apertures and typically 4×10^{10} dots cm^{-2} about four QDs are detected. Further selection is achieved spectrally, and an unambiguous assignment of spectral lines to a single specific QD is provided by exploiting the omnipresent effect of spectral diffusion [26].

Single-dot spectra allow to gain insight into the Coulomb-affected few-particle properties. An important aspect of Coulomb interaction is the renormalization of few-particle transition energies occurring when an electron and a hole confined in a QD recombine in the presence of additional charge carriers. The biexciton binding energy is of particular interest for applications, e.g. for emitters of polarization-entangled single-photon pairs from excitonic and biexcitonic transitions. Its value is given by the energy difference between excitonic and biexcitonic recombination. Representative spectra of a large and a small InAs/GaAs QD are shown in Fig. 3.16. The different excitonic transitions within a single QD spectrum were identified via polarization and excitation dependend measurements [21]. Due to the statistical nature of carrier capture into the dots emission from neutral excitons (X), biexcitons (XX), as well as from charged excitonic complexes are observed in the studied case.

A remarkable feature of the spectra of a large and a small dot in Fig. 3.16 is the reversed order of exciton and biexciton emission. Another apparent feature discussed in Section 3.3 is the large fine-structure splitting of the large dot's exciton emission in the upper spectrum compared to the small splitting of the small dot.

For a systematic investigation of the relation between excitonic binding energies and structural properties of the QDs many single-dot spectra were recorded all over

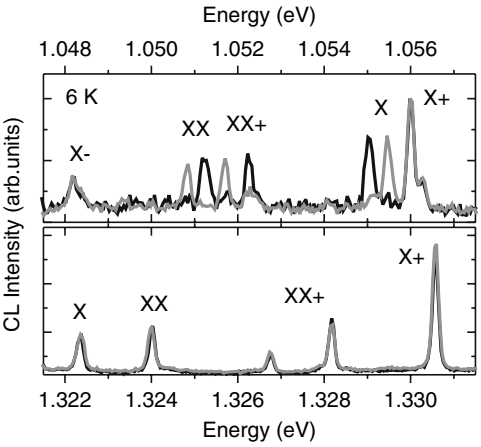

Fig. 3.16 Catholdoluminescence spectra of a single large (top) and a small dot (bottom), linearly polarized along [$\bar{1}$10] (π^+, black spectra) and [110] (π^-, grey spectra). From [27]

the inhomogenously broadened ensemble peak. The resulting binding energies for the biexciton and the two trions are plotted in Fig. 3.17 as a function of the neutral exciton recombination energy. There exist apparent characteristic trends and energy regimes for the three excitonic complexes. The negatively charged exciton (also termed negative trion) has always a positive binding energy, i.e. the emission is shifted to the red, $\mathrm{E(X)} - \mathrm{E(X^-)} > 0$. In contrast to this behavior, the binding energies of the biexciton and the positive trion decrease as the exciton energy increases, i.e. the dot gets smaller. The energy of the biexciton even changes from binding to antibinding.

The binding energies originate from the Coulomb interaction between the confined charge carriers. This interaction is discussed in terms of direct Coulomb interaction and correlation to understand the observed trends. The energy regimes of the two trions can be explained by the direct Coulomb interaction alone [28]. The negative trion $\mathrm{X^-}$ consists of two electrons and one hole confined in the QD. Its binding energy directly depends on the difference between the two direct Coulomb terms $C(e,h)$ and $C(e,e)$. The binding energy of the positive trion $\mathrm{X^+}$ correspondingly depends on $C(e,h)$ and $C(h,h)$. Due to the larger effective mass of holes and the small size of the QDs the wave function of the hole is stronger localized than that of the electron, cf. wave functions in Fig. 3.15. Consequently $|C(e,e)| < |C(e,h)| < |C(h,h)|$, and the negative trion has a positive binding energy, while the positive trion has a negative binding energy.

As to the trends of the binding energies the effect of correlation is to be considered. To model the impact of correlation the number of confined QD states for electrons and holes included in the calculation was varied [28]. The procedure is motivated by the observation in Fig. 3.12 that the number of confined states decreases for increasing ground-state recombination energy, i.e. for smaller dots. In the numerical model the number of bound states is expressed by the size of the function basis, i.e. the number of electron and hole levels used to build the exciton basis-states for

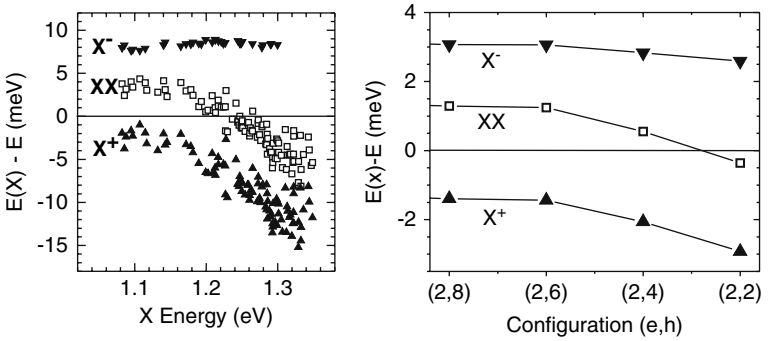

Fig. 3.17 Left: Energy distances between the recombination energy of confined exciton complexes and that of the neutral single exciton as a function of the single exciton emission energy. Right: Calculated energy distances of the recombination energy of confined exciton complexes with respect to that of the neutral single exciton as a function of the number of states included in the configuration interaction. After [28]

the CI calculation. By comparing calculations for different configurations it became obvious that the number of bound *hole* levels is the main factor governing the trend of the binding energies. The right panel of Fig. 3.17 shows the result of calculations where the number of electron states is kept constant at two and the number of hole levels is varied from eight for large QDs to two for small QDs. Obviously the trends and energy regimes observed in the experiment are well reproduced.

The study on single quantum dots demonstrates that the order of binding energies of confined few-particle complexes is controlled by the mutual direct Coulomb interaction. The magnitude of the binding energies depends on the size of the quantum dots and is governed by the number of bound states.

3.3.3 Anisotropic Exchange Interaction

The polarized spectra of a large and a small QD in Fig. 3.16 showed a splitting of the neutral exciton and biexciton transitions. Both emissions are split into two lines of equal intensity, and in both cases the order of their polarization with respect to the transition energy is reversed. The splitting of these emissions is identical. This more clearly recognizable in Fig. 3.18 which shows the respective emissions of two other single QDs. The splitting is defined to be positive if the (110) polarization appears at lower energy in the exciton doublet, i.e. the X line at lower energy is π^+ polarized. In Fig. 3.18 positive and negative splittings can be observed. The other polarization-dependend lines appearing in Fig. 3.16 which originate from the recombination of the positively charged biexciton and the positive trion change intensity as a function of polarization direction. All these features originate from the anisotropic part of the exchange interaction among the confined electrons and holes and are discussed in the following.

The identical, so-called fine-structure splitting (FSS) of the exciton and biexciton emissions results from a lifting of the degeneracy of the bright exciton state, which

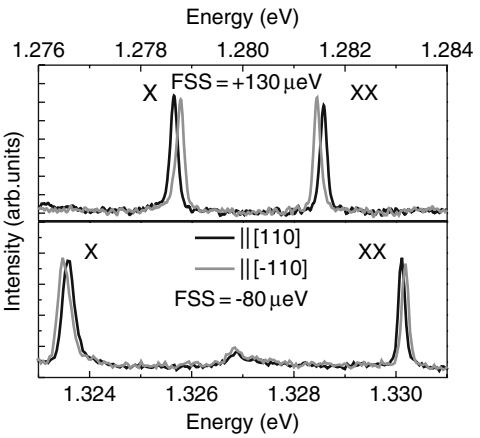

Fig. 3.18 Polarized spectra of two quantum dots with reversed order of polarization in the exciton emission

is the final state of the biexciton decay and the initial state of the exciton decay. Its origin is the exchange interaction, which couples the spins of electrons and holes, and their Zeeman interaction with internal and external magnetic fields [29]. Since the Zeeman contribution is generally negligible in absence of an external magnetic field it will not be considered here. We focus on the exciton ground state in crystals with zincblende structure like InAs and GaAs which have T_d point group symmetry.

The exciton consits of an electron and a hole. Only heavy-hole states are considered for simplification, though the calculations presented below include light-hole and split-off hole contributions. The ground state is then composed of angular-momentum projections $s_z = \pm 1/2$ and $j_z = \pm 3/2$, yielding four exciton states with momentum projections M_z equal to ± 1 and ± 2. In absence of Coulomb interaction and band- and spin-coupling effects, the exciton ground state is hence fourfold degenerate due to four combinations of products $e_i h_j$ with $i, j \in \{1, 2\}$. The two-particle Hamiltonian can be expanded into a basis of antisymmetrized product wave functions

$$e_i(\mathbf{r}_1)h_j(\mathbf{r}_2) \rightarrow \frac{1}{\sqrt{2}}\left(e_i(\mathbf{r}_1)h_j(\mathbf{r}_2) - h_j(\mathbf{r}_1)e_i(\mathbf{r}_2)\right) \quad i, j \in \{1, 2\}\,. \tag{3.7}$$

The degeneracy of the four exciton states with M_z equal to $(|1\rangle, |-1\rangle, |2\rangle, |-2\rangle)$ is lifted by the Coulomb interaction as depicted in Fig. 3.19. The Coulomb interaction consists of direct and exchange terms and reads in the basis of Eq. (3.7)

$$(C \cdot \mathbf{1} + \begin{pmatrix} 0 & \Delta_B & 0 & 0 \\ \Delta_B & 0 & 0 & 0 \\ 0 & 0 & -K & \Delta_D \\ 0 & 0 & \Delta_D & -K \end{pmatrix}) u = E_i u. \tag{3.8}$$

C is the direct Coulomb term $\langle e_i h_j | H_{Coul} | e_i h_j \rangle$ and K is the diagonal exchange term $\langle e_i h_j | H_{Coul} | h_j e_i \rangle$. Solving this equation results in the eigenvectors and eigenstates

$$(E_1, E_2, E_3, E_4) = (\underbrace{C - K - \Delta_D, C - K + \Delta_D}_{D}, \underbrace{C - \Delta_B, C + \Delta_B}_{B}). \tag{3.9}$$

The index D marks states with $|M_z| = 2$. These states do not couple to photon fields and are usually not intermixed with the $|M_z| = 1$ states in absence of magnetic fields. Therefore they are generally not observed in luminescence experiments and denoted *dark* states. The two dark states are split by $E_2 - E_1 = 2\Delta_D$. The splitting is accompanied by the formation of symmetric and antisymmetric linear combinations $|2\rangle + |-2\rangle$ and $|2\rangle - |-2\rangle$ of the pure spin states 2. The states with indices B are correspondingly formed by linear combinations $|1\rangle + |-1\rangle$ and $|1\rangle - |-1\rangle$ and are referred to as *bright* states. The difference $E_4 - E_3 = 2\Delta_B$ is called bright splitting or fine-structure splitting. If the confining potential has a high symmetry (at least C_{4v}) then Δ_B is equal 0 and the wave functions are pure spin states 1. This is not

the case for a confinement in a quantum dot, even if the shape of the dot is that of a square-based pyramid like those considered in this chapter. Piezoelectric effects lead to a reduction of the symmetry to C_{2v} [22, 24]. The experimentally observed splitting shown in Fig. 3.16 with linear polarizations oriented along (110) demonstrates that the actual dot symmetry is C_{2v}. The symmetry lowering also causes the pure spin states in C_{4v} symmetry to mix, and the corresponding circularly polarized transitions become linearly polarized in C_{2v} as shown in Fig. 3.19. The two directions of polarization are perpendicular to each other and reflect the symmetry characteristics of the confining potential. The biexciton state corresponds to $M_z = 0$ and is therefore not split by exchange interaction. Since the single exciton is the final state in the XX $\rightarrow$ X transition, this emission also reflects the fine-structure splitting and mixing of the bright-exciton spin states.

The single dot spectra given in Figs. 3.16 and 3.18 suggest that the magnitude of exchange interaction is related to the size of QDs. For a systematic analysis spectra of a large number of QDs with different sized were studied. Figure 3.20 compiles fine-structure splittings as a function of the single-exciton recombination energy which is directly related to the size of the dots. The exciton fine-structure splitting increases from small negative values for small QDs to positive values as large as 520 μeV for large QDs within the multimodal dot ensemble, as indicated by bars on top. Such large splittings reported in Ref. [30] were usually not observed for InAs/GaAs QDs by other groups [e.g.[29, 31, 32, 33]]. The dependence shown in Fig. 3.20 clearly confirms that the magnitude of the exciton fine-structure splitting scales with QD size.

The action of the anisotropic exchange interaction is also reflected in the recombination of the positively charged biexciton and the positive trion. Their emissions were shown in Fig. 3.16 to change intensity and the direction of polarization for different single QDs. The systematic effect of size on the action of the anisotropic exchange in the exciton fine-structure splitting raises the question if such dependence also exists for the charged biexciton and trion. A scheme of the charged-biexciton decay is shown in Fig. 3.21.

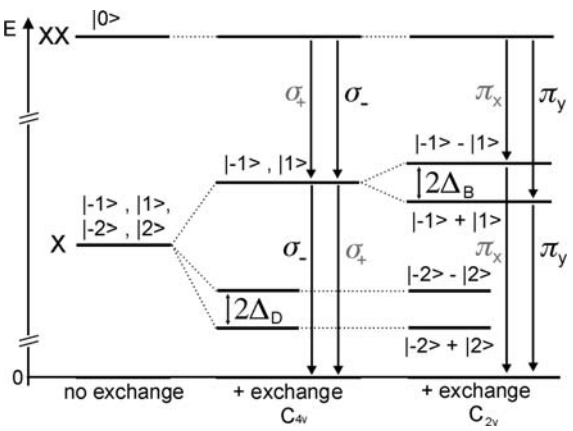

Fig. 3.19 Energy scheme of exciton and biexciton states, illustrating the effect of exchange interaction and symmetry of the confining potential. $2\Delta_D$ and $2\Delta_B$ mark the splittings of dark ($|\pm 2\rangle$) and bright ($|\pm 1\rangle$) states, $\sigma_{+/-}$ and $\pi_{x/y}$ denote circular and linear polarization, respectively

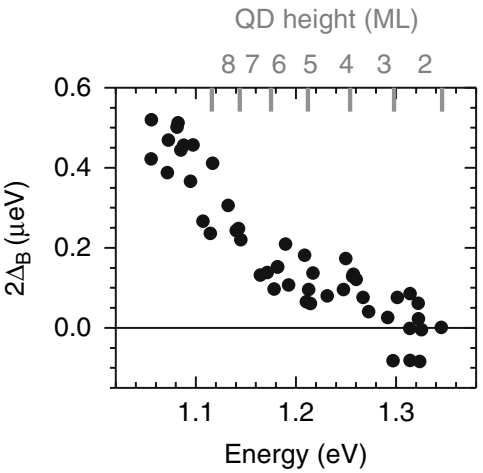

Fig. 3.20 Magnitude of the exciton fine-structure splitting $2\Delta_B$ for a number of InAs/GaAs quantum dots with different sizes. PL maxima of subensembles are marked by grey bars on top

The initial XX^+ state of the cascade is degenerate, analogous to the case of the neutral biexciton. The final state of the positive trion (X+*) comprises one singlet and three triplet states which are all twofold degenerate [34]. Contrary to the exciton case, this degeneracy is not lifted under exchange interaction. The exchange interaction leads to a mixing of the triplet states and alters the initially pure circular polarization to elliptic polarization. The degree of polarization of these lines hence reflects the degree of intermixing of the different charged trion states and therefore the magnitude of the anisotropic exchange interaction. The change of the polarization of the two XX^+ recombination lines from circular for pure states to elliptic, i.e. the degree of mixing of the trion states, is defined by the polarization degree

$$p = \frac{I^{\pi+} - I^{\pi-}}{I^{\pi+} + I^{\pi-}}. \tag{3.10}$$

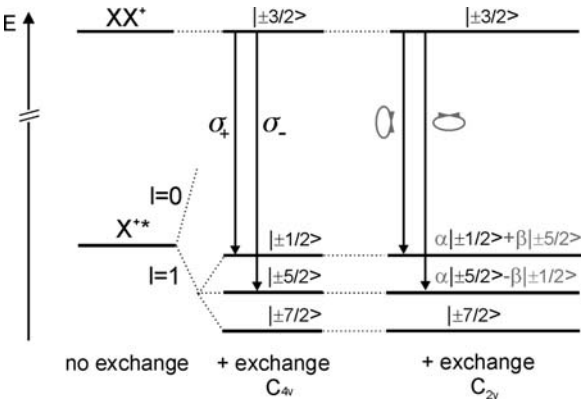

Fig. 3.21 Energy scheme of the charged-bieciton to charged-exciton decay. Grey features indicate changes by the anisotropic exchange interaction, ellipses indicate elliptic polarization. X^{+*} singlet states are omitted for clarity

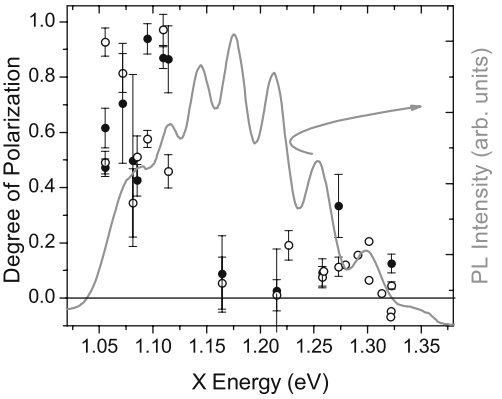

Fig. 3.22 Degree of polarization of the two emission lines of the positive-biexciton decay. The grey spectrum represents the photoluminescence of the QD ensemble. Circles and dots refer to the two different polarizations of the split emission lines. From [37]

Data of the polarization degree as measured all over the inhomogeneously broadened QD ensemble emission are given in Fig. 3.22 [37]. They show that also the polarization of the positive-biexciton to trion decay follows a systematic trend with the size of QDs.

The measurements clearly demonstrate the impact of the anisotropic part in the exchange interaction on electrons and holes confined in a QD. Such anisotropy arises in the dots, when the symmetry of the confining potential is lower than C_{4v}. Sources for such symmetry lowering are structural anisotropy of the dots, piezoelectricity induced by strain [22, 24], and atomistic symmetry anisotropy [35]. Structural elongation of the studied quantum dots can be ruled out as a main source for the observed exchange effects. TEM measurements outlined in Section 2.3 do not show a significant anisotropy, and numerical modeling fails to reproduce experimental results [30]. Moreover, the data demonstrate that the effect of exchange scales with the size of the QDs. Piezoelectricity provides a possible explanation for the observed trend [30]. Its magnitude is proportional to the occurring shear strain in the QDs. Due to the lattice mismatch between GaAs and InAs, the shear strain is larger for larger QDs [24]. Larger QDs with stronger shear strain components hence lead to stronger piezoelectric fields. Consequently such QDs have larger values of the fine-structure splitting, and the XX^+ lines show a larger degree of polarization. Though the experimentally observed scaling trend of the fine-structure splitting was well reproduced by first-order calculations of piezoelectricity [30], the magnitude was not. Furthermore, the importance of second order terms in the piezoelectric effect was recently pointed out [36]. Linear and quadratic terms were shown to have an opposite effect, and the quadratic term may dominate for large strains. The role of atomistic symmetry anisotropy is not yet studied in detail. A major contribution cannot be excluded in a complete treatment of exchange interaction in quantum dots.

3.4 Conclusion

Control of strained-layer deposition in the Stranski-Krastanow mode can be employed to fabricate equally-shaped InAs quantum dots in GaAs matrix with a well-defined multimodal distribution of sizes. Growth studies demonstrate that such dots form from a rough quantum well and ripen by a material exchange between dots of different subensembles. The evolution is theoretically described by an interplay of the strain energy in the dots and the chemical potential of the adatom sea.

The well-defined structure of the InAs/GaAs quantum dots has enabled a systematic study of the complex interplay between Coulomb interaction and confining potential for confined charge carriers. An apparent dependence of excitonic properties on the size of the quantum dots is found. The bright-exciton fine-structure splitting changes monotonously from negative values to more than 0.5 meV and the biexciton binding energy varies from -6 meV to 4 meV, i.e. from antibinding to binding, as the height of the truncated pyramidal dots increases from 2 to above 9 InAs monolayers. The binding energies of charged and neutral excitons increase due to correlation by the gradually increasing number of bound states for increasing dot size. The increasing magnitude of the fine-structure splitting with dot size is caused by the anisotropic part of the exchange interaction, with major contributions from the strain-induced piezoelectricity. The identification of key parameters allows to tailor exciton properties, providing a basis for applications of quantum dots in novel devices.

References

1. M. Grundmann (Ed.), *Nano-Optoelectronics*, Springer, Berlin (2002).
2. D. Leonard, K. Pond, P.M. Petroff, Phys. Rev. B **50**, 11687 (1994).
3. A. J. Bennett, D. C. Unitt, A. J. Shields, P. Atkinson, K. Cooper, D. A. Ritchie, Appl. Phys. Lett. **86**, 181102 (2005).
4. U.W. Pohl, K. Pötschke, A. Schliwa, F. Guffarth, D. Bimberg, N.D. Zakharov, P. Werner, M.B. Lifshits, V.A. Shchukin, D.E. Jesson, Phys. Rev. B **72,** 245332 (2005).
5. M. Grundmann, J. Christen, N.N. Ledentsov, J. Böhrer, D. Bimberg, S.S. Ruvimov, P. Werner, U. Richter, U. Gösele, J. Heydenreich, V.M. Ustinov, A.Yu. Egorov, A.E. Zhukov, P.S. Kop'ev, Zh.I. Alferov, Phys. Rev. Lett. **74,** 4043 (1995).
6. J.F. Carlin, R. Houdré, A. Rudra, M. Ilegems, Appl. Phys. Lett. **59**, 3018 (1991).
7. A. Gustafsson, D. Hessmann, L. Samuelson, J.F. Carlin, R. Houdré, A. Rudra, J. Crystal Growth **147,** 27 (1995).
8. S. Raymond, S. Studenikin, S.-J. Cheng, M. Pioro-Ladrière, M. Ciorga, P.J. Poole, M.D. Robertson, Semicond. Sci. Technol. **18,** 385 (2003).
9. U.W. Pohl, K. Pötschke, M.B. Lifshits, V.A. Shchukin, D.E. Jesson, D. Bimberg, Appl. Surf. Sci. **252**, 5555 (2006).
10. R. Heitz, F. Guffarth, K. Pötschke, A. Schliwa, D. Bimberg, N.D. Zakharov, P. Werner, Phys. Rev. B **71**, 045325 (2005).
11. R. Sellin, F. Heinrichsdorff. Ch. Ribbat, M. Grundmann, U.W. Pohl, D. Bimberg, J. Crystal Growth **221,** 581 (2000).

12. U. W. Pohl, K. Pötschke, I. Kaiander, J.-T. Zettler, D. Bimberg, J. Crystal Growth **272,** 143 (2004).
13. J.-T. Zettler, J. Rumberg, K. Ploska, K. Stahrenberg, M. Pristovsek, W. Richter, M. Wassermeier, P. Schützendübe, J. Behrend, L. Däweritz, Phys. Stat. Sol (a) **152,** 35 (1995).
14. U.W. Pohl, K. Pötschke, A. Schliwa, M.B. Lifshits, V.A. Shchukin, D.E. Jesson, D. Bimberg, Physica E **32**, 9 (2006).
15. R. Timm, H. Eisele, A. Lenz, T.-Y. Kim, F. Streicher, K. Pötschke, U.W. Pohl, D. Bimberg, M. Dähne , Physica E **32**, 25 (2006).
16. N. Moll, M. Scheffler, E. Pehlke, Phys. Rev. B **58**, 4566 (1998).
17. Q. K. K. Liu, N. Moll, M. Scheffler, E. Pehlke, Phys. Rev. B **60**, 17008 (1999).
18. G. Costantini, C. Manzano, R. Songmuang, O.G. Schmidt, K. Kern, Appl. Phys. Lett. **82**, 3194 (2003).
19. G. Costantini, A. Rastelli, C. Manzano, P. Acosta-Diaz, R. Songmuang, G. Katsaros, O.G. Schmidt, K. Kern, Phys. Rev. Lett. **96**, 226106 (2006).
20. J. Drucker, Phys. Rev. B **48**, 18203 (1993).
21. S. Rodt, R. Seguin, A. Schliwa, F. Guffarth, K. Pötschke, U.W. Pohl, D. Bimberg, J. Lumin. **122-123**, 735 (2007).
22. O. Stier, M. Grundmann, D. Bimberg, Phys. Rev. B **59,** 5688 (1999).
23. O. Stier, R. Heitz, A. Schliwa, D. Bimberg, Phys. Stat. Sol. (a) **190**, 477 (2002).
24. M. Grundmann, O. Stier, D. Bimberg, Phys. Rev. B **52,** 11969 (1995).
25. M. Sugawara, Phys. Rev. B **51**, 10743 (1995).
26. V. Türck, S. Rodt, O. Stier, R. Heitz, R. Engelhardt, U.W. Pohl, D. Bimberg, R. Steingrüber, Phys. Rev. B **61** (2000) 9944.
27. U.W. Pohl, R. Seguin, S. Rodt, A. Schliwa, K. Pötschke, D. Bimberg, Physica E **35**, 285 (2006).
28. S. Rodt, A. Schliwa, K. Pötschke, F. Guffarth, D. Bimberg, Phys. Rev. B **71,** 155325 (2005).
29. M. Bayer, G. Ortner, O. Stern, A. Kuther, A.A. Gorbunov, A. Forchel, P. Hawrylak, S. Fafard, K. Hinzer, T.L. Reinecke, S.N. Walck, J.P. Reithmaier, F. Klopf, F. Schäfer, Phys. Rev. B **65**, 195315 (2002).
30. R. Seguin, A. Schliwa, S. Rodt, K. Pötschke, U.W. Pohl, D. Bimberg, Phys. Rev. Lett. **95**, 257402 (2005).
31. K. Kowalik, O. Krebs, A. Lemaître, S. Laurent, P. Senellart, P. Voisin, J.A. Gaj, Appl. Phys. Lett. **86,** 041907 (2005).
32. A.S. Lenihan, M.V. Gurudev Dutt, D.G. Steel, S. Gosh, P.K. Bhattacharya, Phys. Rev. Lett. **88,** 223601 (2002).
33. R.J. Young, R.M. Stevenson, A.J. Shields, P. Atkinson, K. Cooper, D.A. Ritchie, K.M. Groom, A.I. Tartakovskii, M.S. Skolnick, Phys. Rev. B **72**, 113305 (2005).
34. K.V. Kavokin, Phys. Stat. Sol. (a) **195**, 592 (2003).
35. G. Bester, S. Nair, A. Zunger, Phys. Rev. B **67**, R161306 (2003).
36. G. Bester, X. Wu, D. Vanderbilt, A. Zunger, Phys. Rev. Lett. **96**, 187602 (2006).
37. R. Seguin, S. Rodt, A. Schliwa, K. Pötschke, U.W. Pohl, D. Bimberg, Phys. Stat. Sol. (b) **243**, 3937 (2006).